Materials & Design 235 (2023) 112429

Contents lists available at ScienceDirect

Materials & Design

journal homepage: www.elsevier.com/locate/matdes

Implementation of time of flight polarized neutron imaging at IMAT-ISIS

U.K. Oji [a,b,*], V. Pacheco [c], M. Sahlberg [c], A. Backs [d], R. Woracek [d], D.E. Pooley [e], G.J. Nilsen [e], K. Nemkovski [e], W. Kockelmann [e], A.S. Tremsin [f], A. Hilger [b], R. Ziesche [b], I. Manke [b], R. Cubitt [a], N. Kardjilov [b]

[a] Institut Laue-Langevin, Large Scale Structures Group, 71 avenue des Martyrs CS 20156, 38042, Grenoble Cedex 9, France
[b] Helmholtz-Zentrum Berlin für Materialien und Energie (HZB), D-14109 Berlin, Germany
[c] Department of Chemistry – Ångström Laboratory, Uppsala University, Box 523, SE-75120 Uppsala, Sweden
[d] European Spallation Source ERIC, Box 176, 22100 Lund, Sweden
[e] STFC, Rutherford Appleton Laboratory, ISIS Facility, Chilton OX11 0QX, UK
[f] Space Sciences Laboratory, University of California at Berkeley, Berkeley, CA 94720, USA

ARTICLE INFO

Keywords:
Additive manufacturing
Polarized neutron imaging
Magnetic structures

ABSTRACT

In this study, we report the first case of design and implementation of a polarized neutron imaging option on the Imaging and Materials Science & Engineering Station (IMAT). This is a significant addition to the capabilities of the station that allows the characterization of advanced magnetic materials for different engineering applications. Combining its time-of-flight feature with a polarized beam yields data that facilitate both quantitative and qualitative analysis of magnetic materials. Using the simple field of an aluminium solenoid, we perform a characterization of the new setup. In addition, we present polarized measurements of additively manufactured (AM) MnAl samples where the magnetic anisotropy due to the fabrication process has been investigated as a first scientific application of the setup. The results indicate that the anisotropy of the material can be engineered through variation of the AM fabrication parameters.

1. Introduction

Neutron imaging is a well-established technique used for visualization and non-destructive characterization of internal structures in objects and devices. The Imaging and Materials Science & Engineering station (IMAT) [1] is situated at the Rutherford Appleton Laboratory in Oxfordshire, United Kingdom as one of 30 neutron instruments of the ISIS Neutron & Muon Source. Facilitated by the pulsed nature of the neutron source at ISIS, IMAT utilizes the time-of-flight (TOF) method allowing it to be used for energy resolved imaging experiments in a variety of materials science and engineering research areas. Transmission spectra of neutrons in radiographic images or tomographic volumes can be further analyzed to obtain physical quantities or microstrucural distributions in a sample [2,3]. IMAT has attracted attention in the research field of materials characterization due to its time-of-flight capabilities for mapping materials' structural properties such as residual strains in metals [4] and crystallographic phase fractions in battery electrodes [5].

Neutrons can be used for magnetic characterization as well resulting from their spin property and charge neutrality. To date, there are variety of studies that evidence the neutron's capability for magnetic characterization via scattering experiments with spin-polarized and non spin-polarized neutron beams [6]. In the same vein, for neutron imaging, both polarized and non-polarized neutron beams have facilitated studies using radiography/tomography techniques [7,8] and grating interferometry [9] respectively. Consequently, combining a polarized neutron beam with the TOF feature of the IMAT imaging station for radiography opens up the opportunity for both qualitative and quantitative studies of magnetic fields and materials facilitated by the wavelength resolving power of TOF measurements.

In this paper, we report on the implementation of a polarized neutron imaging option at the IMAT imaging station. Calibration of the setup is achieved using an electromagnetic coil taking advantage of the TOF feature. Furthermore, investigations are carried out on additively manufactured samples of MnAl to determine the potential of the fabrication technique in production of MnAl with a controlled anisotropy of

* Corresponding author at: Institut Laue-Langevin, Large Scale Structures Group, 71 avenue des Martyrs CS 20156, 38042, Grenoble Cedex 9, France; Helmholtz-Zentrum Berlin für Materialien und Energie (HZB), D-14109 Berlin, Germany.
E-mail address: u.oji@campus.tu-berlin.de (U.K. Oji).

https://doi.org/10.1016/j.matdes.2023.112429
Received 18 July 2023; Received in revised form 14 October 2023; Accepted 24 October 2023
Available online 26 October 2023

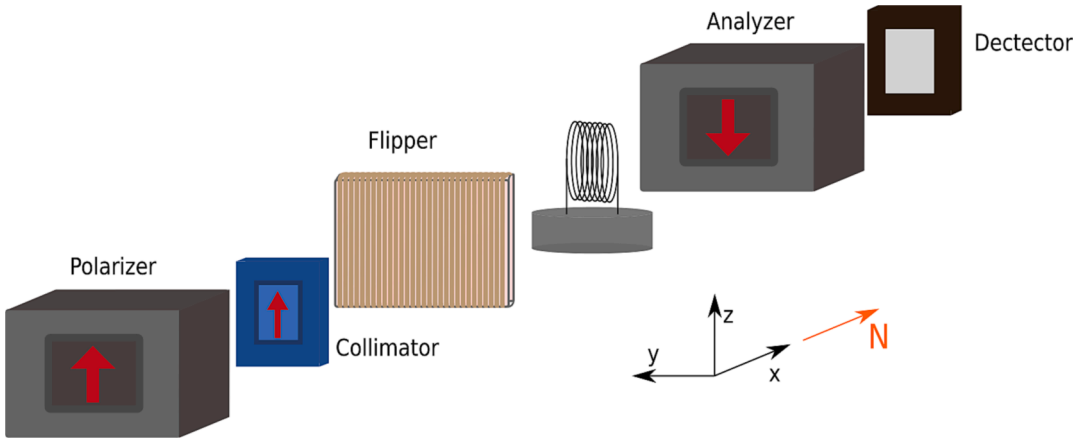

Fig. 1. Schematic of the Polarized Neutron Imaging Implementation on the IMAT beamline.

the magnetic domains.

1.1. Polarized neutron imaging

Neutrons, possessing a magnetic moment due to their spin, interact with magnetic fields. This interaction directly affects the spin property and can lead to modifications of the neutron velocity or trajectory in the presence of strong enough field gradients [10]. The average value of the spins of a neutron ensemble, being the case for a neutron beam, is the polarization of the beam. This property can be shown to behave just like a classical moment [11]. Analogous to the case of a single neutron spin, the polarization precesses in a magnetic field with an axis in the direction of the field. This process is called a Larmor precession and occurs with an angular frequency

$$\omega = \gamma B \tag{1}$$

where B is the magnetic flux density of the field and γ is the neutron gyromagnetic ratio. A neutron beam traversing a distance of x through a uniform magnetic field in the time, t, will have a total precession angle of

$$d\theta = \omega t = \omega \frac{x}{v} = \gamma \frac{\lambda m}{h} Bx \tag{2}$$

with v being the velocity of the neutron, λ being the de Broglie wavelength and $m = 1.675 \times 10^{-27}$ kg being the neutron rest mass. From the equations above, two variables are important for imaging with polarized neutrons based on their relation with the total precession angle: the neutron wavelength and the magnetic field strength. The implication is that a measurement of the total precession angle gives information of the path integral of the magnetic field strength along the trajectory of a monochromatic neutron beam. While the total precession angle cannot be measured directly, we can measure a scalar projection spin polarization of the neutron beam along a given axis expressed as

$$P = \frac{N\uparrow - N\downarrow}{N\uparrow + N\downarrow} \tag{3}$$

where $N_\uparrow$ and $N_\downarrow$ are the intensities from two separate measurements, with the initial polarization being flipped by 180 degrees in the latter case, commonly referred to as spin up ($N_\uparrow$) and spin down ($N_\downarrow$) respectively. This value, depends on the precession angle, which is in turn proportional to the neutron wavelength. In this way P has an oscillatory relationship with the neutron wavelength.

$$P = \cos(\theta) \tag{4}$$

$$P = cos\left(\gamma \frac{\lambda m}{h} \int Bdx\right) \tag{5}$$

The above relationship allows for the determination of the magnetic field strength through the neutron trajectory from the change of the neutron wavelength without requiring a direct precession angle measurement. This represents a major advantage of performing polarized neutron imaging at a pulsed spallation neutron source over reactors as the time of flight (TOF) technique facilitates the measurements of the polarization change for different wavelengths.

1.2. Setup

The setup of the experiment is illustrated in Fig. 1 and the choices for the components and their modes of operation are outlined below. The setup comprises a polarizer with (an additional) collimator, a spin flipper, a sample, a polarization analyzer and a pixellated 2D detector.

1.3. ISIS-IMAT

The IMAT imaging station of ISIS had been chosen for this polarized neutron imaging study due to its energy resolved imaging ability. Due to the pulsed nature of the neutron source, wavelength-resolved spectra can be obtained via TOF analysis and utilized for polarized neutron imaging experiments, thus facilitating quantitative and qualitative characterization of magnetic fields and materials [12]. A setup on a pulsed source presents a major advantage to polarized neutron imaging at reactor sources where extra components such as a double crystal monochromator requires installation and an additional wavelength scan to achieve the same goal. On a TOF instrument a wide wavelength range with fine TOF binning is achieved from the start of the data collection which facilitates in-situ studies and concomitant Bragg edge analysis of microstructural properties.

The instrument used a 'pinhole setup', with a circular neutron collimator of D = 80 mm about L ≈ 10.4 m upstream of the transmission detector. This geometry defines a quasi-parallel neutron beam, with a divergence determined by an L/D of about 130. The wavelength range was 0.7 to 6.7 A. A TOF-capable pixel detector was setup 10.5 m downstream of the pinhole position then synchronized to the 10 Hz pulsed neutron source of the ISIS second target station. A 0.25 mm thick GS1 glass scintillation TOF monitor was used for setting up the components. A GP2 detector (pixel size: 70 um), based on neutron conversion in a Gd-conversion foil and CMOS charge-readout [13] was used for optimizing the setup, and a MCP detector (pixel size: 55 um), based on neutron conversion in a Gd and B doped microchannel plate and Timepix readout [14], was used for recording wavelength resolved neutron images on MnAl samples.

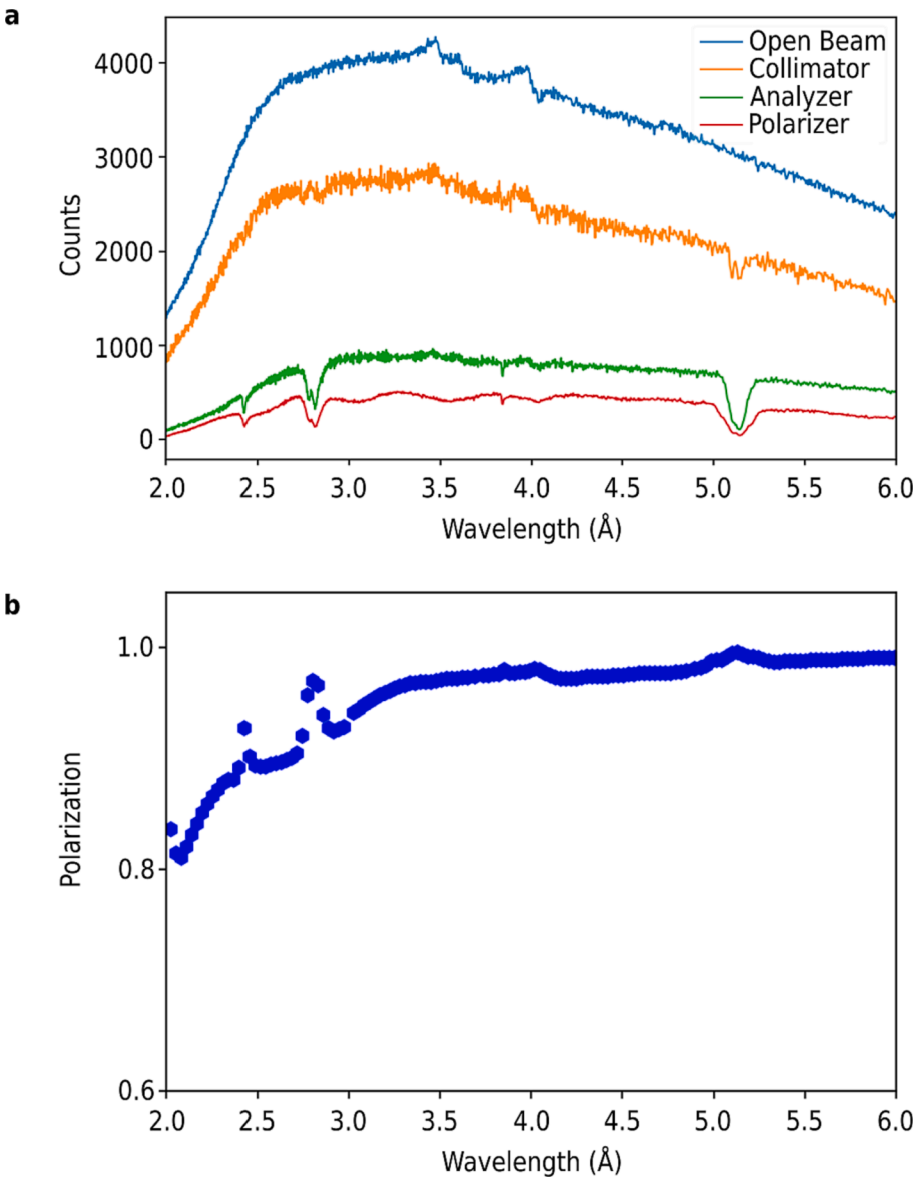

Fig. 2. (a) TOF transmission signal after installation of the solid state polarization devices measured with a TOF monitor. There is approximately 90 % loss of neutron flux with the final polarized neutron imaging setup. The dips observed at 2.4 Å, 2.8 Å and 5.2 Å are Bragg dips resulting from Silicon in the components (b) Time of Flight polarization signal of the open polarized neutron beam. The setup produces a mean polarization of 95 % ± 0.05.

1.4. Polarization devices

The devices for polarization and analysis of the neutron beam are an essential part of a polarized neutron imaging setup. Compactness and a large field of view for the neutron beam are important properties to be considered for the choice of polarization devices. This is to ensure that sufficient spatial image resolution is obtained by minimizing the sample-to-detector distance and that a sufficiently large polarized neutron beam is provided to interact with the magnetic field inside a sample. Furthermore, a wide band of neutron wavelengths is desired to analyze magnetic fields. Especially in the case of small fields characterizations, having a weak wavelength dependence necessitates the use of polarizing devices optimized to the neutron spectrum of the beam line/instrument. Considering the requirements, solid state benders have been used as polarization-analysis devices for the setup. For the polarizer, a polarizing transmission bender was used with dimensions of 30 mm × 50 mm with a length of 120 mm. The coatings are polarizing super-mirrors made of Fe/Si and the substrate is single crystal Si wafer of thickness 0.15 mm. The mirrors have a critical angle relative to nickel (m-value) of 3.3 and the critical neutron wavelength for these polarizing devices is 2.1 Å. This critical wavelength stays below the peak neutron flux wavelength of 2.6 Å on IMAT which allows efficient polarized neutron imaging at the imaging station [1].

The magnetic polarizing mirrors are aligned vertically. They work in transmission meaning that only one spin channel is transmitted, which we define as spin up, while the other channel (spin down) is reflected. A magnetic housing made of Nd-based permanent magnets applies a field of 600 G which magnetizes the super-mirror [15,16]. The analyzing mirror operates similarly to the polarizer with the main difference being that it works in reflection. This results from the gadolinium coating on the backside of its silicon lamellae, which directly absorbs the non-reflected neutrons. The polarizer is used in combination with a Soller collimator consisting of stacked TiGd (0.25 μm) coated Si (0.3 mm) wafers. The angular adjustment of the collimator allows transmission of either the transmitted or the reflected neutron spin component and to remove the other one. In our case the collimator was set to retain the transmitted spin channel and provided an angular divergence of 0.34° in the horizontal and 1.28° in the vertical direction.

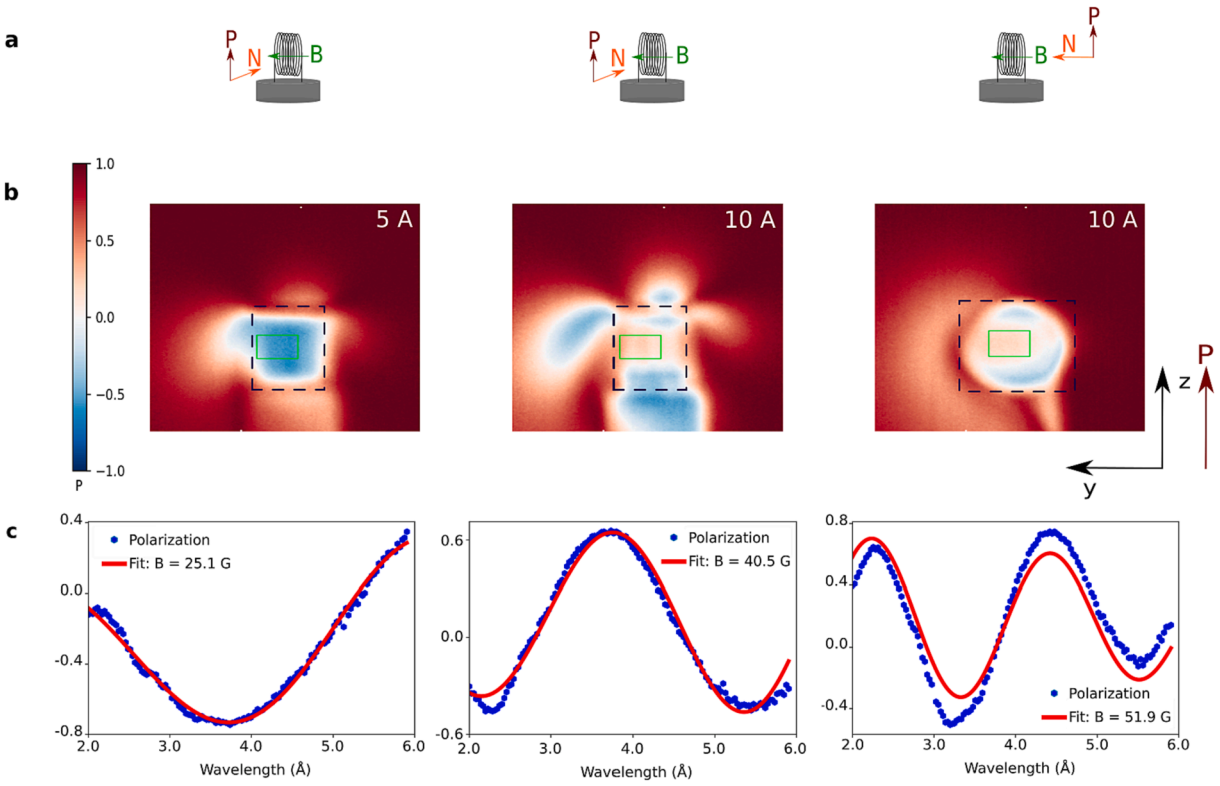

Fig. 3. (a) Schematic illustration of the configuration of the solenoid with respect to the neutron beam direction and polarization (b) Corresponding polarized neutron images of Aluminium coil of diameter = 10.5 mm, length = 12 mm and 5 turns integrated through wavelengths 2–6 Å measured as a function of current and orientation: 5 A, 10 A and 10 A after 90° rotation through the z axis. (c) Corresponding TOF polarization signal from the green boxed region fitted to the aforementioned function to determine the magnitudes of homogeneous field produced. Black dashed lines indicate the coil outline and the signal in (b) is obtained from the solid green region.

Table 1
Printing conditions for M_{05} and M_{07}.

	M_{07}	M_{05}
Powder	$(Mn_{60.7}Al_{39.3})_{100}C_{2.8}$	$(Mn_{54.9}Al_{45.1})_{100}C_{3.9}$ $V_{0.9}$
Laser Power	20 W	20 W
Laser Speed	220 mm/s	180 mm/s
Hatch Spacing	0.07 mm	0.05 mm
Print process	Double melt, single direction	Double melt, orthogonal directions

1.5. Spin rotators

A Mezei coil rotator was installed for controlling the neutron polarization direction. The device works by using a static magnetic field orthogonal to the neutron beam polarization direction for non-adiabatic rotation of the spin orientation. The field strength for polarization rotation is adjustable by varying the current flowing through the coils and a compensating field coil was included to reduce the stray field at the flipper position. For the use at IMAT, the current was swept in synchronization with the neutron pulses [17]. This makes the Mezei rotator suitable for flipping the orientation of neutrons over a wide range of neutron wavelengths.

1.6. Effect on flux

Installation of each polarization device leads to a reduction of the neutron flux at the detector position. The selection of one spin channel, efficiency of the supermirrors and attenuation in the silicon lamellae reduce the initial flux to approximately 10 %. This is illustrated in Fig. 2. Despite the reduction in flux, high quality polarized TOF data could be obtained in a reasonable time scale.

1.7. MCP detector

The detector used in the MnAl was the microchannel plate detector (MCP) developed by the University of California at Berkeley [14]. For the use with neutrons, the MCP glass is doped with boron and gadolinium, which are responsible for the neutron capture and subsequent generation of secondary electrons. The electronic signal is amplified within the pores, localized to an area of about 10 μm. This signal is read out by an application specific integration chip (ASIC) referred to as Timepix. This chip allows for neutron event mode data collection important to TOF imaging.

The detector has a pixel size of 55 μm × 55 μm with 512 × 512 pixels. This gives the detector an effective field of view of 28 mm × 28 mm. At 320 μs, the readout time of the integrated electronics enables acquisition of multiple TOF ranges within each neutron pulse with individually controlled time resolution within each shutter.

1.8. Setup and calibration

The devices were installed in the sequence of collimator, analyzer, polarizer and spin flipper illustrated in Fig. 1. With exception of the spin flipper, the components were mounted on rotation stages. For the collimator and spin analyzer, these were used to align the devices to maximum transmission, with a precision of 0.1°. Its calibration was performed similarly to the analyzer to maximize transmission with rotations through angular steps of 0.1°.

Similarly, the spin polarizer was aligned for maximum beam polarization via a modified shim-test. For this, a 0.5 mm Fe sheet was installed to cover part of the beam. The Fe sheet completely depolarizes the initially polarized beam. The polarizer was rotated through angular steps of 0.1° with the objective of maximizing the contrast between the

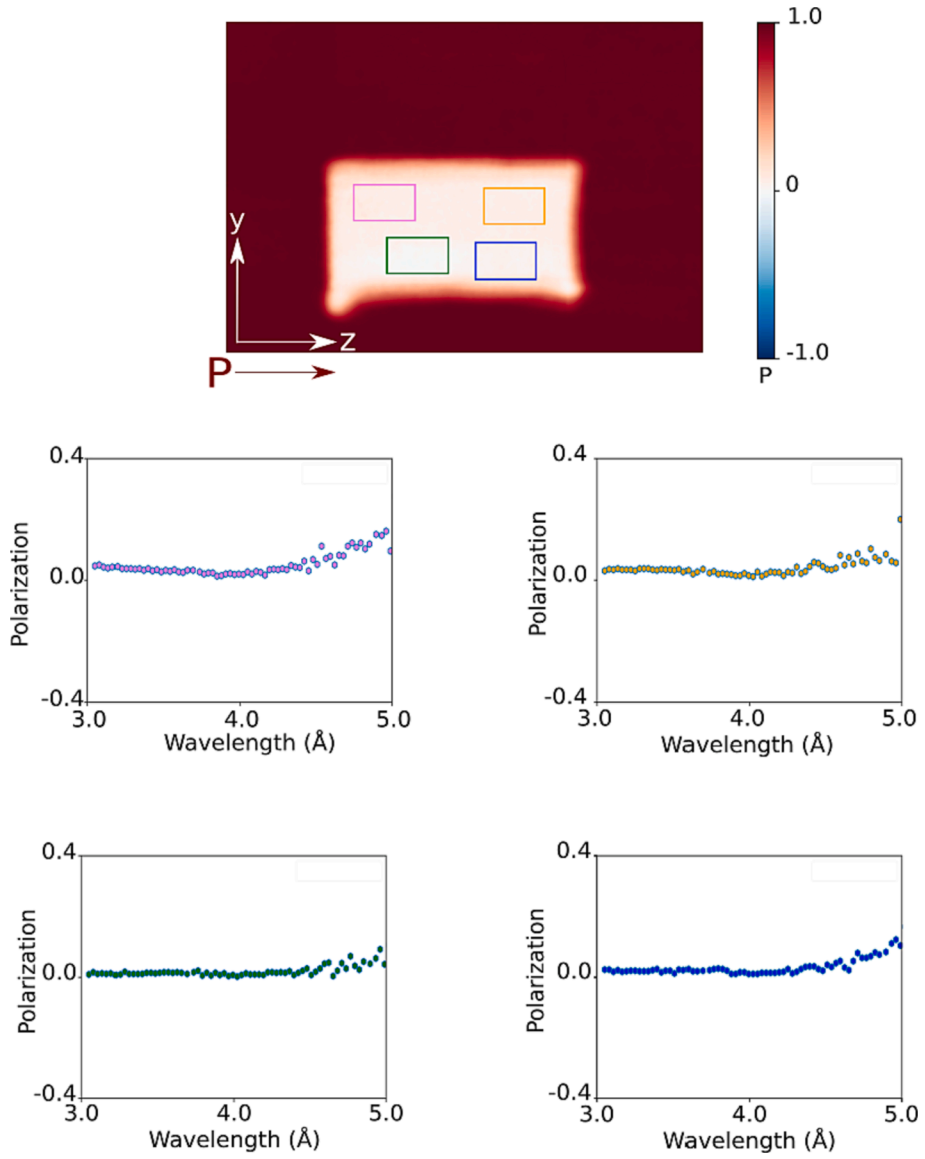

Fig. 4. TOF polarization signal of boxed regions in M_{07}. The complete depolarization of the neutron beam through the wavelength range is an indication of high levels of inhomogeneity of the magnetic moments orientations in the sample.

regions of the sheet and the empty beam. Finally, the spin flipper was installed and its current profile calibrated for their effective use in TOF polarized neutron imaging. The average polarization of the beam through the TOF was determined to be 95 % with a standard deviation of 0.05. The polarized neutron beam is guided using a combination of the fields from the benders and dedicated guide fields equipped with the Mezei flippers. These guide fields are oriented in the z axis through the neutron beam trajectory, confirmed using a magnaprobe compass and were found to be effective in maintaining the degree of the neutron beam polarization for the experiment duration. With the inclusion of the collimator, the effective horizontal L/D of the experiment was about 200.

2. Experiment

2.1. Solenoid

For calibration of the polarized imaging setup, we have used a small aluminium solenoid as a sample which provides a comparatively simple magnetic field. The coil was wound by hand with a length of 12 mm, an outer diameter of 10.5 mm and 5 turns. It is made from 1 mm Aluminium wire to avoid neutron absorption, which was below the detectable threshold. Positioned 25 cm away from the detector, currents of 5 A and 10 A were applied through the coil resulting in generated magnetic fields in the center of the coil of 21 G and 42 G, respectively, oriented along the coil's axis measured using a Hall probe. The coil axis was aligned in two orientations perpendicular to the neutron polarization; perpendicular and parallel to the neutron beam (c.f. Fig. 3), in order to maximize the spin rotation.

Radiographs for the various configurations were taken with the exposure time for each spin channel being 15 min. We can assume that most of the spin rotation occurs inside the solenoid, where the field is strong and homogeneous, while contributions from the far reaching stray field are comparatively weak. Accordingly, equation (5) can be used to determine the field strength from the TOF Polarization data which we can compare with the Hall probe measurements.

Fig. 3 shows results of the polarization measurements alongside sketches of the corresponding geometric setup in the top row. In panel (b) wavelength integrated radiographs are given with the position of the coil marked by a black dashed rectangle and the corresponding

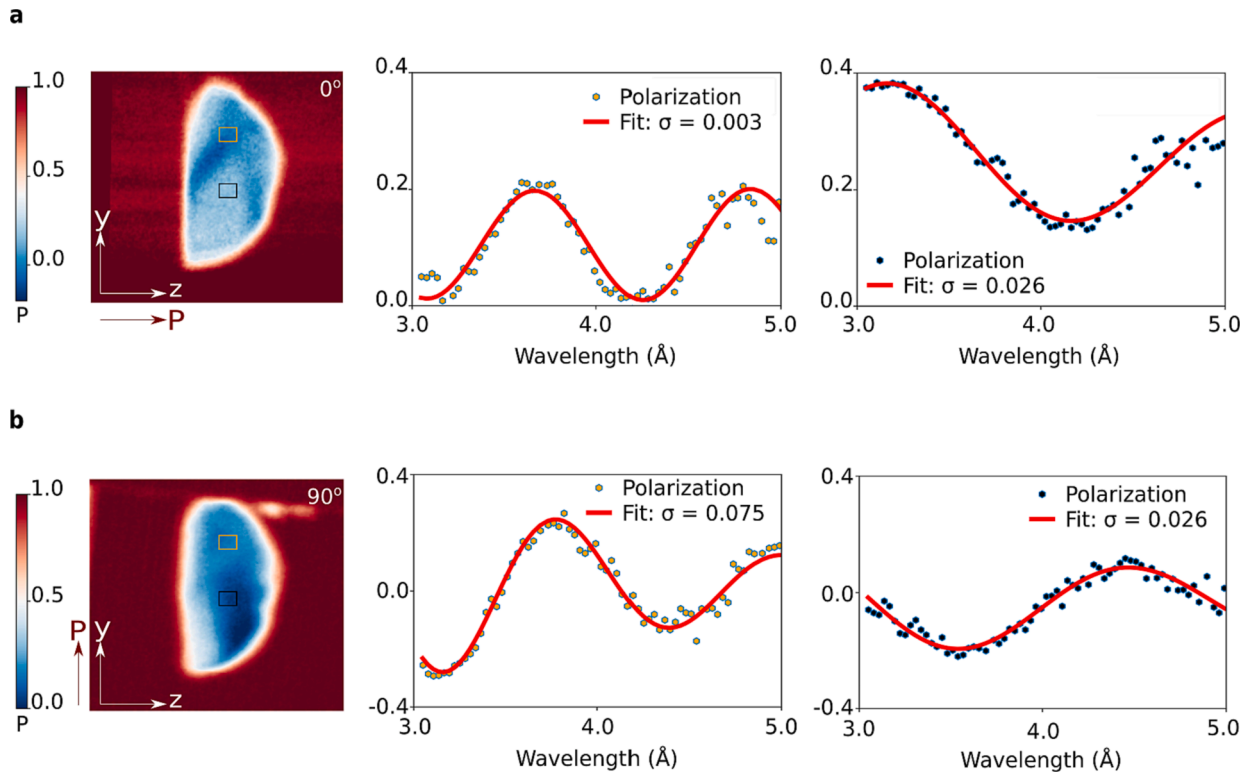

Fig. 5. TOF polarization signals for selected regions of the additively manufactured MnAl M_{05}. In general there is not a complete depolarization of the beam indicating a level of homogeneity of the magnetic domains and ultimately a general anisotropy. This is seen from the TOF polarization of the highlighted regions while the sample is (a) not rotated and (b) rotated around the x axis by 90°. The effect of damping from inhomogeneity of the magnetic domains seems to be more pronounced for (a) than (b) in the blue and green regions.

configuration of the coil with respect to the neutron beam direction and polarization shown in (a). Panel (c) shows TOF data evaluated in the regions indicated by green rectangles in panel (b). It is immediately visible, that higher currents, and the associated higher magnetic field, created more oscillations in the polarization spectrum. In addition, we observe a further increase of the oscillation frequency for the parallel coil orientation. This is expected, since the perpendicular orientation includes a field reversal between the outer and inner field of the coil, while this feature is absent in the parallel alignment. With equation (5), the field strength has been determined for the three measurements as 25.1 G (5 A, perpendicular), 40.5 G (10 A, perpendicular) and 51.9 G (10 A parallel). To determine the field strength, we have assumed the dimensions of the coil as the flight path of the neutrons through the coil's generated field; 10.5 mm and 12 mm for the perpendicular and parallel arrangements. These values are in fair agreement with the Hall-probe measurements, especially due to the described simplifications. Simulations of the fields and spin rotation for comparison are included in the supplementary information.

2.2. Additively manufactured MnAl

Additive manufacturing (AM) of MnAl is the fabrication method most likely to give it a competitive chance in the permanent magnets market [18]. With a theoretical energy product, $(BH)_{max}$, of 112 kJ/m^3 [19,20], MnAl permanent magnets would have the potential to fill the gap in the market between applications demanding materials with a $(BH)_{max}$ of 31.8 kJ/m^3 [19,21] occupied by hard ferrites and those that require a $(BH)_{max}$ of 397.8 kJ/m^3 [19,21,22] occupied by Nd-Fe-B magnets. A major drawback in its adoption is the difficulty/cost associated with mass production of MnAl magnets with magnetic anisotropy. In the past, fairly suitable MnAl magnets have been manufactured via warm extrusion [23] however this method ultimately was found not to be sustainable due to the cost of extrusion dye replacement coupled with difficulties in magnetic anisotropy control. Exploring AM as a fabrication method improves the chances of effectively controlling the magnetocrystalline anistropy [18]. This results from the direct effects of AM parameters such as hatch distance, scanning speed and laser power on the crystallographic properties of the fabricated MnAl. In the following, we explore the effect of different printing conditions on the orientation of the resulting moments in two samples of additively manufactured MnAl. The objective of this particular study of additively manufactured MnAl was to determine the viability of AM in the fabrication of MnAl with a controlled anisotropy. TOF polarized neutron imaging is an ideal characterization technique due to the neutron precession's dependence on the direction of the magnetic field in combination with the wavelength dependence of the final polarization after precession.

Polarized neutron images were obtained for the two samples of AM MnAl studied. The samples shall henceforth be referred to as M_{05} and M_{07} and the information on their AM fabrication is shown in Table 1. M_{05} is a solid semi-circle with radius 3.5 mm and thickness of 3 mm while M_{07} is a cuboid with a face of dimension 5 mm × 10 mm and thickness 5 mm. For the experiment, the samples are positioned at a distance of 5 cm away from the analyzing mirror. In this position, the guiding magnetic field has a value of about 200 G. This position does not only help to improve the spatial resolution obtained but has a secondary objective of suppressing the stray field visualization from the sample. This suppression is achieved from the adiabatic coupling of the neutron beam polarization with the combination of the stray field from the sample and the guiding magnetic field. The guide field at this position should not have a significant effect on the samples' internal moment orientation due to its high coercive field (see supplementary information). This effectively guarantees that any changes in contrast seen in the visualized image is mostly a result of the neutron depolarization/precession with the internal magnetic flux of the sample. Exposure time for

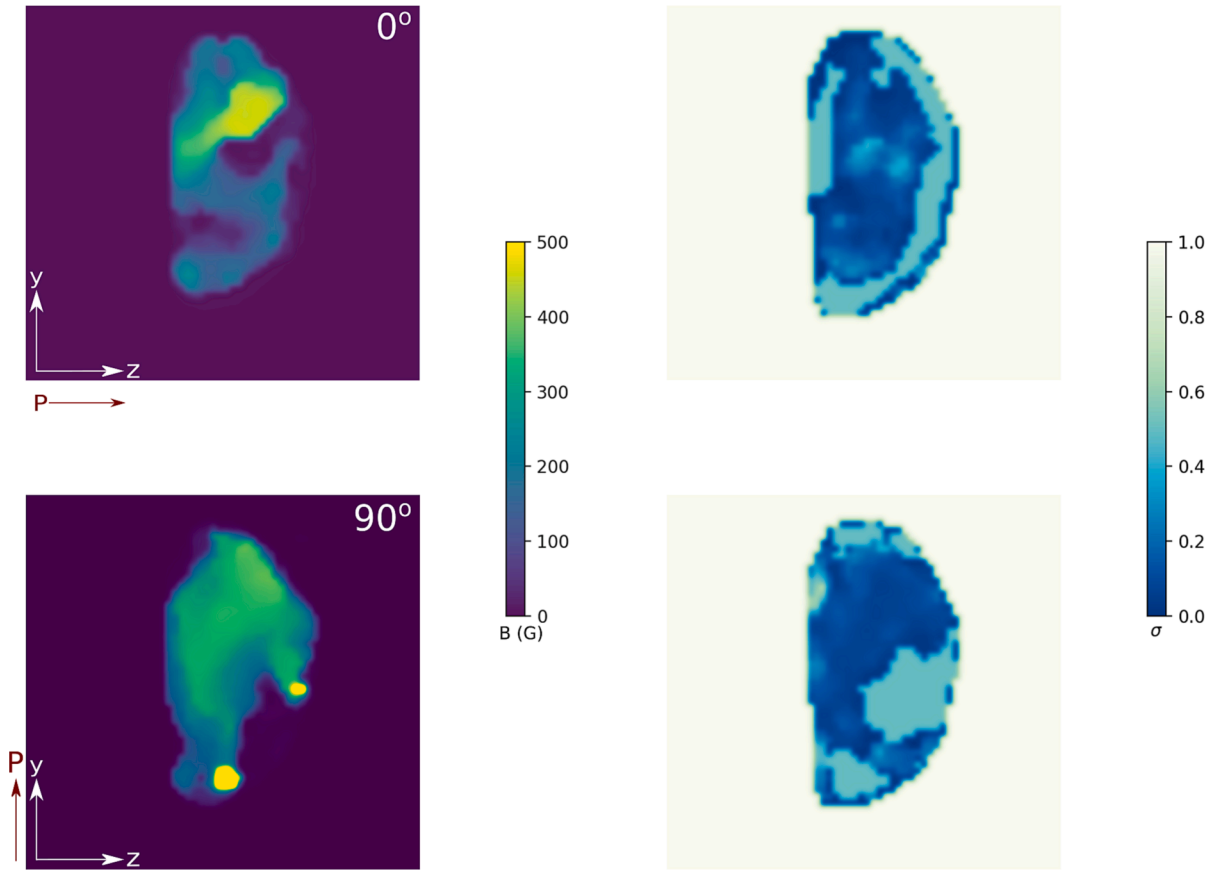

Fig. 6. Colour map of the σ values to show the level of homogeneity of the magnetic domains in the sample M_{05}. Lower σ values indicate a higher homogeneity of magnetic domains. $\sigma_{mean} = 0.23$ Å $^{-2}$ and 0.2 Å $^{-2}$ with standard deviations of 0.2 and 0.18 for the 0° & 90° cases respectively.

each radiograph is 60 mins.

Fig. 4 shows the TOF signal for M_{07} from the highlighted regions. In all cases, the neutron beam becomes completely depolarized after interaction with the sample. This complete depolarization of the beam is an indication that while the sample is magnetic, the magnetic domains are inhomogeneous and the internal moments of the domain do not have a preferential orientation direction. In contrast to this, a look at the TOF signal from the highlighted regions of M_{05} (Fig. 5(a)) makes it evident that while the sample does result in depolarization of the beam, there is a precession signal. This precession signal is the main indication of a preferential moment orientation for the domains in the sample. Based on the relative orientations of the sample and neutron polarization, it can be inferred that the moments of the domains in these regions have a significant projection in the x-y plane direction that allows for the precession signal observed. Taking advantage of the wavelength dependence of the total precession, quantitative information on the level of domain homogeneity can be obtained. These are done via fitting the TOF signal to the function [24,25]

$$y = Ae^{-\sigma\lambda^2} cos(\omega\lambda) + c \tag{6}$$

where A is the amplitude of the sinusoidal TOF signal, ω is the angular frequency and c is the offset. The principle parameters obtained from the fit are σ and ω where σ is a parameter related to the inhomogeneity of the domains through the neutron flight path and ω facilitates the determination of magnetic field strength (B) values being that frequency of the signal is a direct consequence of the magnitude of B in the characterized material. The determined σ values are 0.003 Å^{-2}, 0.026 Å^{-2} for the orange and blue regions respectively. Lower values of σ indicate higher homogeneity in the sampled regions. The corresponding values of B determined for the regions are 232 G and 135 G.

The sample was rotated by 90° around the x axis and the polarized neutron images are obtained for this configuration. This rotation of the sample by 90 degrees is equivalent to the rotation of the incident neutron beam polarization by 90 degrees around the same axis and is henceforth represented as such for the purpose of clarity. Fig. 5(b) shows the TOF signal of the polarization for highlighted regions in the new configuration. In this case, the polarization was interacting primarily with moment projections in the x-z plane. The values of σ are determined to be 0.075 Å^{-2}, 0.026 Å^{-2} for the orange and blue regions respectively. The corresponding value of B determined are 219 G and 145 G. The difference in the mean value of B in the highlighted regions of the sample are likely a result of differences in the phase distribution of MnAl in these regions post heat treatment.

To get a more global view of the sample's magnetic properties, a map of the sample's internal field and the sigma values are plotted in Fig. 6. The polarized neutron images through TOF are 4 × 4 pixel binned to obtain better statistics for the analysis. There is a discrepancy in the maps of B determined by the method for the both orientations as can be seen from Fig. 6. This is a consequence of the direction dependent process via which the neutron polarization interacts with a magnetic field. This does not directly answer the question of a preferred moment orientation in the sample however a comparison of the sigma maps can facilitate an understanding of the magnetic moment orientations.

In the cases of 0° and 90° sample orientations, there seems to be more regions of lower homogeneity domains for the former which could indicate a preferred orientation for the internal moments. Taking the mean of the σ (σ_{mean}) values resulting for each orientation is a method for quantification of the global homogeneity of the moments for each orientation. σ_{mean} has values of 0.23 Å^{-2} with standard deviation of 0.2 and 0.2 Å^{-2} with a standard deviation of 0.18 for 0° and 90° orientations respectively. The lower value of σ_{mean} in the 90° case in addition to the

apparently more homogeneous distribution of sigma values in the Fig. 6 suggest that the sample has magnetic domains whose internal moments have orientations with significant projections on the x-z plane indicating a level of magnetic anisotropy. From these results, it can be concluded that additive manufacturing is a viable method for fabrication of MnAl permanent magnets via which the magnetic anisotropy can be engineered through a modification of the scanning parameters. This observation in M_{05} is possibly from higher density of the sample due to the scanning parameters chosen for the AM process such as the lower hatch distance, the slower scan speed and scan strategy [26,27,28]. This higher density and hence higher order of compactness should lead to a higher energy required for disordering of the magnetic moments in the τ phase. Additional studies have shown that the small compositional difference between the sample do not significantly affect the differences in texture or microstructure of the samples and these factors are determined mostly by the scanning parameters [29,30].

3. Conclusion

Polarized Neutron Imaging has been implemented on the ISIS IMAT beamline for the first time using solid state polarizing devices. The beam polarization obtained through TOF reached a mean of 95 %. Combining a polarized beam and the TOF capability of the instrument, it was possible to determine the magnitude of a homogeneous magnetic field serving as a proof of the technique's viability on the IMAT beamline. Furthermore, the setup made possible a study of the effects of additive manufacturing methods on the anisotropy of MnAl. The studies serve to highlight the importance of scanning parameters in the determination of the magnetic ordering and homogeneity of the final product. Specific to our case, we infer, based on the directional dependence of the neutron precession in a magnetic field, that the magnetic moments of the MnAl fabricated using a lower hatch distance in combination to a multidirectional scanning technique and lower scan speeds have more significant projections on the x-z plane for the sample suggesting a level of anisotropy in the sample. This information will be instrumental in the optimization of the growth process to maximize the magnetic anisotropy in samples from future iterations. Future studies of the magnets with a full polarimetric imaging setup will give more detailed information of their magnetic anisotropy.

Declaration of Competing Interest

The authors declare the following financial interests/personal relationships which may be considered as potential competing interests: Martin Sahlberg reports financial support was provided by Swedish Foundation for Strategic Research. Martin Sahlberg reports financial support was provided by Swedish Research Council.

Data availability

Data will be made available on request.

Acknowledgements

We are grateful for the support by M. Devonport (ISIS Polarisation Group), J. Lewis (ISIS Mechanical Support Group) and J. Nutter (ISIS Electrical Support and Motion Control). The STFC Rutherford Appleton Laboratory is thanked for access to neutron beam facilities (IMAT/RB2210226, DOI 10.5286/ISIS.E.RB2210226). Instrumentation development for this project was jointly funded by the Institut Laue Langevin, the Helmholtz Zentrum Berlin and ISIS Neutron and Muon Source. MnAl research is funded by the Swedish Foundation for Strategic Research (SSF) within the Swedish national graduate school in neutron scattering (SwedNess) and by the Swedish Research Council (#2022-03069).

Appendix A. Supplementary data

Supplementary data to this article can be found online at https://doi.org/10.1016/j.matdes.2023.112429.

References

[1] W. Kockelmann, T. Minniti, D. Pooley, G. Burca, R. Ramadhan, F. Akeroyd, G. Howells, C. Moreton-Smith, D. Keymer, J. Kelleher, S. Kabra, T. Lee, R. Zi- esche, A. Reid, G. Vitucci, G. Gorini, D. Micieli, R. Agostino, V. Formoso, F. Aliotta, R. Ponterio, S. Trusso, G. Salvato, C. Vasi, F. Grazzi, K. Watanabe, J. Lee, A. Tremsin, J. McPhate, D. Nixon, N. Draper, W. Halcrow, J. Nightin- gale, Time-of-Flight Neutron Imaging on IMAT@ISIS: A New User Facility for Materials Science, Journal of Imaging 4 (3) (2018) 47. doi:10.3390/ jimaging4030047.

[2] R. Woracek, J. Santisteban, A. Fedrigo, M. Strobl, Diffraction in neutron imaging—a review, Nucl. Instrum. Methods Phys. Res., Sect. A 878 (2018) 141–158, https://doi.org/10.1016/j.nima.2017.07.040.

[3] H. Sato, T. Kamiyama, Y. Kiyanagi, A rietveld-type analysis code for pulsed neutron bragg-edge transmission imaging and quantitative evaluation of texture and microstructure of a welded α-iron plate, Mater. Trans. 52 (6) (2011) 1294–1302, https://doi.org/10.2320/matertrans. M2010328.

[4] R.S. Ramadhan, D. Glaser, H. Soyama, W. Kockelmann, T. Shinohara, T. Pirling, M. E. Fitzpatrick, A.S. Tremsin, Mechanical surface treatment studies by Bragg edge neutron imaging, Acta Mater. 239 (2022), 118259, https://doi.org/10.1016/j.actamat.2022.118259.

[5] R.F. Ziesche, A.S. Tremsin, C. Huang, C. Tan, P.S. Grant, M. Storm, D.J.L. Brett, P. R. Shearing, W. Kockelmann, 4D Bragg edge tomography of directional ice templated graphite electrodes, Journal of Imaging 6 (12) (2020) 136, https://doi.org/10.3390/jimaging6120136.

[6] S. Mühlbauer, D. Honecker, É.A. Périgo, F. Bergner, S. Disch, A. Heinemann, S. Erokhin, D. Berkov, C. Leighton, M.R. Eskildsen, A. Michels, Magnetic small-angle neutron scattering, Rev. Mod. Phys. 91 (1) (2019), 015004, https://doi.org/10.1103/RevModPhys.91.015004.

[7] N. Kardjilov, I. Manke, M. Strobl, A. Hilger, W. Treimer, M. Meissner, T. Krist, J. Banhart, Three-dimensional imaging of magnetic fields with polarized neutrons, Nat. Phys. 4 (5) (2008) 399–403, https://doi.org/10.1038/nphys912.

[8] A. Hilger, I. Manke, N. Kardjilov, M. Osenberg, H. Markötter, J. Banhart, Tensorial neutron tomography of three-dimensional magnetic vector fields in bulk materials, Nat. Commun. 9 (1) (2018) 4023. doi:10.1038/ s41467-018-06593-4.

[9] T. Neuwirth, A. Backs, A. Gustschin, S. Vogt, F. Pfeiffer, P. Böni, M. Schulz, A high visibility Talbot-Lau neutron grating interferometer to investigate stress- induced magnetic degradation in electrical steel, Sci. Rep. 10 (1) (2020) 1764, https://doi.org/10.1038/s41598-020-58504-7.

[10] T. Oku, H. Iwase, T. Shinohara, S. Yamada, K. Hirota, S. Koizumi, J.-i. Suzuki, T. Hashimoto, H. M. Shimizu, A focusing-geometry small-angle neutron scattering instrument with a magnetic neutron lens, J. Appl. Crystallogr. 40 (s1) (2007) s408–s413. doi:10.1107/S0021889807003822.

[11] J.T. Cremer, Introduction, in: Neutron and X-ray Optics, Elsevier, 2013, pp. 1–160, 10.1016/B978-0-12-407164-3.00019-X.

[12] T. Shinohara, K. Sakai, M. Ohi, T. Kai, M. Harada, K. Oikawa, F. Maekawa, J. Suzuki, T. Oku, S. Takata, K. Aizawa, M. Arai, Y. Kiyanagi, Quantitative magnetic field imaging by polarized pulsed neutrons at J-PARC, Nucl. Instrum. Methods Phys. Res. Section A 651 (1) (2011) 121–125, https://doi.org/10.1016/j.nima.2011.01.099.

[13] D. E. Pooley, J. W. Lee, F. Akeroyd, O. Arnold, M. Hart, J. J. John, P. M. Kadletz, W. Kockelmann, T. Minniti, C. Moreton-Smith, M. Morgano, N. J. Rhodes, E. M. Schooneveld, I. Sedgwick, C. Vallance, R. Woracek, Energy Resolved Imaging using the GP2 Detector: Progress in Instrumentation, Methods and Data Analysis, in: Neutron Radiography, 2020, pp. 35–41. doi: 10.21741/9781644900574-6.

[14] A.S. Tremsin, J.V. Vallerga, J.B. McPhate, O.H.W. Siegmund, R. Raffanti, High resolution photon counting with MCP-timepix quad parallel readout operating at > 1 KHz frame rates, IEEE Trans. Nucl. Sci. 60 (2) (2013) 578–585, https://doi.org/10.1109/TNS.2012.2223714.

[15] T. Krist, Solid state and conventional neutron optical elements, Nucl. Instrum. 529 (1–3) (2004) 50–53, https://doi.org/10.1016/j.nima.2004.04.175.

[16] T. Krist, F. Mezei, Solid state neutron polarizers and collimators, in: J. L. Wood, I. S. Anderson (Eds.), International Symposium on Optical Science and Technology, San Diego, CA, 2001, pp. 88–95. doi:10.1117/12.448063.

[17] G.J. Nilsen, J. Košata, M. Devonport, P. Galsworthy, R.I. Bewley, D.J. Voneshen, R. Dalgliesh, J.R. Stewart, Polarisation analysis on the LET time- of-flight spectrometer, J. Phys. Conf. Ser. 862 (2017), 012019, https://doi.org/10.1088/1742-6596/862/1/012019.

[18] V. Pacheco, Processing–Structure–Properties Relationship in Metal Additive Manufacturing (Ph.d. Thesis), Acta Universitatis Upsaliensis, 2021, 10.33063/diva-442412.

[19] A. Busachi, J. Erkoyuncu, P. Colegrove, F. Martina, C. Watts, R. Drake, A review of additive manufacturing technology and cost estimation techniques for the defence sector, CIRP J. Manuf. Sci. Technol. 19 (2017) 117–128, https://doi.org/10.1016/j.cirpj.2017.07.001.

[20] J. Coey, Permanent magnets: plugging the gap, Scr. Mater. 67 (6) (2012) 524–529, https://doi.org/10.1016/j.scriptamat.2012.04.036.

[21] A. Gupta, M. Kar, P. Roy, Substitutional effect of Ni-Al in electromagnetic properties of Sr-hexaferrite based non-rare earth magnet with high energy density for

motor applications, Mater. Chem. Phys. 292 (2022), 126842, https://doi.org/10.1016/j.matchemphys.2022.126842.
[22] O. Gutfleisch, Controlling the properties of high energy density permanent magnetic materials by different processing routes, J. Phys. D: Appl. Phys. 33 (17) (2000) R157–R172. doi:10.1088/0022-3727/33/17/201.
[23] Y. Sakamoto, S. Kojima, K. Kojima, T. Ohtani, T. Kubo, Crystal orientation and its formation process of an anisotropic Mn-Al-C permanent magnet, J. Appl. Phys. 50 (B3) (1979) 2355–2357, https://doi.org/10.1063/1.327000.
[24] S. Sasada, K. Hiroi, K. Osanai, T. Shinohara, K. Watanabe, A. Uritani, High- spatial-resolution measurement of magnetization distribution using polarized neutron imaging, Jpn. J. Appl. Phys. 60 (12) (2021), 126003, https://doi.org/10.35848/1347-4065/ac3524.
[25] S. Mitsuda, H. Yoshizawa, Y. Endoh, Neutron-depolarization studies on re-entrant spin glass, Phys. Rev. B 45 (17) (1992) 9788–9797. doi:10.1103/PhysRevB.45.9788.
[26] M. Xia, D. Gu, G. Yu, D. Dai, H. Chen, Q. Shi, Influence of hatch spacing on heat and mass transfer, thermodynamics and laser processability during additive manufacturing of Inconel 718 alloy, Int. J. Machine Tools Manu- Facture 109 (2016) 147–157, https://doi.org/10.1016/j.ijmachtools.2016.07.010.
[27] Z. Dong, Y. Liu, W. Wen, J. Ge, J. Liang, Effect of hatch spacing on melt pool and as-built quality during selective laser melting of stainless steel: modeling and experimental approaches, Materials 12 (1) (2018) 50. doi:10.3390/ ma12010050.
[28] W. Pei, W. Zhengying, C. Zhen, L. Junfeng, Z. Shuzhe, D. Jun, Numeri- cal simulation and parametric analysis of selective laser melting process of AlSi10Mg powder, Appl. Phys. A 123 (8) (2017) 540. doi:10.1007/ s00339-017-1143-7.
[29] D.H.S. Abenayake, Additively Manufactured Rare Earth Free Permanent Mag- nets, Upsalla University, 2023. Ph.D. thesis.
[30] V. Pacheco, B. Skårman, F. Olsson, D. Karlsson, H. Vidarsson, M. Sahlberg, Additive manufacturing of MnAl(C)-magnets, Alloys 2 (2) (2023) 100–109, https://doi.org/10.3390/alloys2020007.